JOINT EUROPEAN TORUS JET

JET–P(92)76

C.D. Challis, T.C. Hender, J. O'Rourke, S. Ali-Arshad, B. Alper, H.J. de Blank, C.G. Gimblett, J. Han, J. Jacquinot, G.J. Kramer, W. Kerner, D.P. O'Brien, P. Smeulders, M. Stamp, D. Stork, P.M. Stubberfield, D. Summers, F. Tibone, B. Tubbing, W. Zwingmann and JET Team

High Bootstrap Current ICRH Plasmas in JET

High Bootstrap Current ICRH Plasmas in JET

C.D. Challis, T.C. Hender[1], J. O'Rourke, S. Ali-Arshad, B. Alper, H.J. de Blank, C.G. Gimblett[1], J. Han[1], J. Jacquinot, G.J. Kramer, W. Kerner, D.P. O'Brien, P. Smeulders, M. Stamp, D. Stork, P.M. Stubberfield, D. Summers, F. Tibone, B. Tubbing, W. Zwingmann and JET Team*

JET-Joint Undertaking, Culham Science Centre, OX14 3DB, Abingdon, UK

[1]UKAEA/Euratom Fusion Association, Culham Laboratory, Abingdon, Oxon, UK
** See Annex*

Preprint of Paper to be submitted for publication in
Nuclear Fusion

HIGH BOOTSTRAP CURRENT ICRH PLASMAS IN JET

C.D.Challis, T.C.Hender*, J.O'Rourke, S.Ali-Arshad, B.Alper, H.J.deBlank, C.G.Gimblett*, J.Han*, J.Jacquinot, G.J.Kramer, W.Kerner, D.P.O'Brien, P.Smeulders, M.Stamp, D.Stork, P.M.Stubberfield, D.Summers, F.Tibone, B.Tubbing, and W.Zwingmann.

JET Joint Undertaking, Abingdon, Oxon, UK.
*UKAEA/EURATOM Fusion Association, Culham Laboratory, Abingdon, Oxon, UK.

ABSTRACT

High poloidal beta plasmas with a correspondingly high bootstrap fraction of $\sim 70\% \pm 15\%$ *have been produced using ion cyclotron resonance heating. This high bootstrap fraction is achieved in an ELM free H-mode confinement regime. This regime is terminated by a large edge instability causing a reversion to L-mode confinement. Possible causes for this edge instability are discussed and the overall implications of these results for steady-state bootstrap dominated operation are examined.*

1 Introduction

The prospects for a steady-state tokamak reactor are significantly enhanced if a substantial fraction of the plasma current can be driven by the neoclassical bootstrap effect [1]. Since the bootstrap current fraction is approximately proportional to the poloidal beta [$\beta_p = 2\mu_0(\int P dv/\int dv)(\int dl/\int B_p dl)^2$], high bootstrap fraction discharges require operation at high-β_p. Previous bootstrap current measurements at TFTR [2], JET [3], and JT-60 [4] with Neutral Beam Injection (NBI) heating have been reported, where a large fraction of the plasma current is attributed to the bootstrap current drive.

Here we present the results of bootstrap current experiments carried out at JET using Ion Cyclotron Resonance Frequency (ICRF) heating. In comparison with experiments using NBI heating these plasmas have negligible central particle fuelling. This is of interest since it has been suggested that there is no bootstrap current in the absence of a plasma outflow [5]. Additionally unlike the previous JET experiments the use of ICRF heating allows the bootstrap current to be studied in the absence of the neutral beam fast ion current. The typical behaviour and characteristics of high-β_p/high-bootstrap discharges in JET are described in Section 2. The current density profile evolution under the influence of the large bootstrap fraction has been studied by several methods, which are discussed in Section 3. Typically the high-β_p phase is terminated by a loss of H-mode and a rapid reduction in β_p. If the heating is maintained after the β_p-reduction the H-mode is rapidly restablished and the cycle of β_p increasing and rapidly decreasing may repeat several times, in some cases. The rapid reduction of β_p is analysed in Section 4. Finally the results are summarised and their implications for steady-state operation with a high bootstrap fraction are discussed in Section 5.

2 Overview of High–β_p Discharges

High–β_p has been achieved by operating with an open divertor H–mode configuration at relatively low current, $I_p \sim 1 - 1.5$MA. For all cases discussed in this paper deuterium double–null X–point discharges were heated with 4–10MW of ICRF heating using a hydrogen minority species and a dipole antenna configuration. A toroidal field of 2.8-3.1T was chosen to allow central heating at 42MHz and to avoid the toroidal β limit. The target plasma electron density was low in these discharges to avoid the density limit at low current (volume averaged density $\langle n_e \rangle \sim 1.0 \times 10^{19}\mathrm{m}^{-3}$) and strong gas puffing was necessary to establish good ICRF coupling. Excessive gas puffing, however, was found to provoke MARFE's or large ELM's which reduced the plasma performance. The coupling resistance ($R_c \simeq 3\Omega$) was maintained using the radial plasma position feedback control [6]. This system was crucial to the success of these experiments since the plasma-antenna separation was small ($\lesssim$ 3cm) in the H-mode phase and the plasma shape and edge conditions varied dramatically in the transition from Ohmic to fully developed high–β_p H-mode plasma.

A typical discharge is shown in Fig. 1. This case has a current of 1MA and a toroidal field of 2.8T with ICRF heating power in the range 6–7MW. In the Ohmic phase immediately preceding the ICRF heating, sawteeth oscillations are visible on the central electron temperature, with a small inversion radius of $\sim$ 15cm. From Fig. 1 it can be seen that these sawtooth oscillations continue for the initial parts of the additionally heated phase ($t < 11.2$s). Low frequency ($\sim$500Hz) quasi–continuous oscillations, characteristic of ICRF fishbones [7], occur during the later sawteeth. During this fishbone/sawtooth phase non-correlated ELM type events are also visible on the D_α–trace. Often these ELM's stop at approximately the same time as the fishbones/sawteeth (though there are discharges in which the sawteeth are absent but the ELM's still occur). Following the cessation of ELM's/fishbones the energy confinement improves and β_p climbs steadily to $\beta_p \sim 2$ where a rapid reduction in β_p occurs. The rapid reduction in β_p, which is related to a reversion to L–mode, is discussed in detail in Section 4. The confinement during the ELM–free phase at best exceeds by 70% the value given by the JET–DIII–D scaling [8], which was, however, derived for ELM–free H-modes at significantly lower edge–q. During the ELM–free phase the density rises monotonically and there is an apparently benign, linearly related increase in radiation to 30–40% of the total input power.

Extended periods of density control were achieved by reducing the heating power during the ELM phase. This provides less transient ELM–free conditions but at the expense of plasma energy and hence bootstrap current. In some cases this technique only serves to delay the density and plasma energy rise. The highest values of β_p were obtained by maintaining high heating powers.

In some discharges (generally those with $I_p = 1.5$MA) the cycle of β_p increasing and then decreasing rapidly, may repeat itself several times. Such a discharge with $I_p = 1.5$MA and $B_T = 2.8$T is shown in Fig. 2. In this case the average β_p per cycle (measured using the diamagnetic loop) is almost 90% of the peak value.

3 Current Density Profile Evolution

The current density profile evolution during the high–β_p phase has been studied using several independent techniques:–

(i) Poloidal field diffusion simulations using the TRANSP code [9].

(ii) Equilibrium reconstructions using the EFITJ [10] and IDENT–D codes [11] which are constrained

to best fit polarimetric (Faraday rotation), magnetic and kinetic measurements.
(iii) Deductions of the q–profile from observed MHD instabilities.

3.1 Poloidal Field Diffusion and Equilibrium Reconstruction

For the TRANSP analysis the effects of neoclassical resistivity and the bootstrap current are included using the measured temperature and density profiles. The bootstrap current calculation [12] neglects the contribution of the fast ion pressure. In the ELM–free H–mode phase where the density rises rapidly, the contribution of the fast ion pressure to the total plasma stored energy is expected to become small ($\sim$10%).

Figure 3 shows (for the same discharge as Fig. 1) the time evolution of the loop voltage ($V_{surface}$), the internal inductance (l_i) and the Faraday rotation angles along three (central) lines of sight as determined experimentally and as simulated by the TRANSP code. Results are shown with and without the bootstrap current included. It can be seen that a good fit to the data is obtained when the bootstrap current is included. In particular, the presence of the bootstrap current leads to a three second period during which the loop voltage is reversed, or close to zero, and to a 30% reduction in l_i, in good agreement with the experimental observations. A bootstrap fraction of $\sim$70% is calculated during the ELM–free phase. For completeness a similar analysis to that shown in Fig. 3 has also been made with Spitzer resistivity alone (no bootstrap terms); in this case $V_{surface}$ is found to remain close to zero from 10s to 12.6s and the agreement with the experimental measurements is not as good as displayed by the neo-classical theory (including the bootstrap terms). Also the Spitzer resistivity is found, even in steady–state, to maintain the central–q significantly above unity in the Ohmic heating phase; a result which is not in accord with the experimental observation of Ohmic sawteeth. Figure 4 shows the same comparison as Fig. 3 of $V_{surface}$, l_i and Faraday rotation angles for a 1.5MA, 3.1T discharge. Although the bootstrap fraction is lower ($\sim$ 50%) in this case, the requirement to include it in order to obtain good agreement, is even more marked. The discharges shown in Figs. 3 and 4 have quite different density behaviour; in the 1MA discharge the density rises sharply during the ELM–free phase (see Fig. 1) whereas for the 1.5MA discharge the density is approximately constant from 10s to 11.5s. Despite this wide variation of density behaviour (and therefore of radial plasma flow) the bootstrap formulation used [12], which essentially relates the bootstrap current to the radial temperature and density gradients, always shows good agreement. In contrast, theories which predict the bootstrap current from its neo-classical relationship to the radial plasma flow (eg. [5]) would clearly have difficulties, particularly in discharges where the density is rising sharply (N.B. gas puffing and edge recycling is the only fuelling source in these discharges). Figure 5 shows the evolution of the calculated bootstrap current for the 1MA discharge shown in Figs. 1 and 3. This calculation is sensitive to the density gradient and temperature close to the plasma boundary, especially during the ELM–free phase. The error bar corresponds to the range of reasonable edge parameters. During the ELM phase the bootstrap current is about 35% of I_p and is distributed across the plasma radius. The suppression of ELM's leads to a four–fold increase in the edge density gradient and a larger bootstrap current, which is however located near the plasma periphery. This change in the bootstrap current density profile (calculated by TRANSP) from the ELM to ELM–free phase is illustrated in Fig. 6. The marked increase in edge current during the ELM–free phase is also confirmed by the equilibrium reconstructions.

The duration of the H–modes in these discharges is not sufficient to reach a steady–state. The diffusion calculations and the equilibrium reconstructions indicate that the central–q (q_0) increases

by no more than 0.4 during the high–β_p phase. This slow diffusion of the central current density during the H–mode phase is due to the high central electron temperature of the discharge and the large radial distance over which the ohmic current perturbation must diffuse (since the bootstrap current is predominantly driven near the edge). As these discharges typically sawtooth until the start of the ELM–free phase, this means that $q_0 \sim 1$ throughout the high–β_p phase. The central–q differs significantly from the steady–state value $q_0 \sim 3$ which would be expected for a bootstrap fraction of 70%.

3.2 Deductions from MHD

An alternate determination of the behaviour of the current density profile arises from the observed instabilities which precede and (sometimes for a short while) follow the rapid reduction in β_p. These instabilities which occur after the ELM phase are observed on the central electron cyclotron emission (ECE) temperature and soft X-ray (SXR) chords. From the toroidal SXR cameras it is found that these instabilities are $n = 1$. The temperature fluctuations from the ECE show an odd–m mode about the plasma centre ($R \sim 3.3$m) with phase reversals near $R = 3.07$ and 3.6m (Fig. 7(a)). These temperature oscillations are very similar to the computed flux surface distortions arising from an $n = 1$ (dominantly $m = 1$) internal kink mode, when the central–q is slightly greater than unity (Fig. 7(b), $q_0 = 1.03$). For the results shown in Fig. 7(b) the linear toroidal stability code FAR [13] has been used to calculate the $n = 1$ eigenfunctions, the amplitude of these eigenfunctions is adjusted to match the observed oscillations, and the mode is assumed to rotate rigidly which gives an equivalence between toroidal angle and time (at a fixed viewing angle). This method provides a relatively sensitive diagnostic of the central q–profile. For $q_0 < 1$ the computed distortions are not in good agreement with the experiment, because of the additional phase inversions due to the $m = 1$ island. While for $q_0 \gtrsim 1.1$ the mode is stable.

A comparison between the observed SXR oscillations and theoretical predictions has also been made. In this case the observed SXR line integrals are reconstructed by assuming constant emissivity on the flux surfaces which are distorted by the computed $n = 1$ eigenfunction. The functional form of the emissivity is adjusted to match the averaged emissivity on each SXR chord. For the equilibrium (with $q_0 = 1.03$) used for Fig. 7(b) the reconstructed SXR chords show excellent relative phase agreement with the experimental measurements (Fig. 8). Direct tomographic reconstruction also gives results consistent with the observed oscillations (Fig. 7(a)) being dominantly $m = 1$ in the core.

3.3 Summary

The transport simulations show a bootstrap current fraction of 70%±15% for an $I_p = 1$MA discharge. Despite this high bootstrap fraction all methods of determining the current density profile suggest that the central current density varies little during the high–β_p phase and that $q(0) \sim 1$ throughout. This slow variation of central current density is partly because the relatively high central temperatures ($T_e(0) \sim 6$keV) mean that there is a long resistive diffusion time in the core, and partly because the bootstrap current is driven primarily in the plasma periphery, thus requiring current diffusion across the entire radius.

4 β_p–decline

There seems to be no correlation between the observed core MHD activity and the rapid β_p-decline. The β_p-decline in fact appears to be related to edge stability, since it is always initiated by a large ELM and appears as an erosion starting from the edge in the SXR profiles. There is also no evidence for the central MHD activity triggering the ELM, as is sometimes observed in high–β discharges [14].

For at least 100msec preceding the β_p-decline the CCD images of one of the ICRF antennas typically show localised heating of the mid-plane edge carbon protection tiles. This strong heating arises because the short scrape–off layer widths in H–mode cause the plasma to be moved towards the plasma antenna, by the position feedback system which maintains the plasma–antenna coupling impedance constant. Also the antenna heating tends to be localised because the outer plasma boundary curvature exceeds that of the antenna at high–β_p. As the density rises during the ELM–free phase the radiated power steadily increases to $\sim 30-40\%$ of the total input power, immediately before the β_p-decline. The dominant radiating impurity is carbon (perhaps from the ICRF antenna) with significant nickel. At the large ELM initiating the β_p-decline, the radiated power fraction increases to $\gtrsim 100\%$, the ICRF coupling to the plasma is lost (Fig. 9), and the plasma reverts to L–mode confinement. The large radiated power causes a rapid decline in temperature but this recovers in ~ 300msec, and the decline in energy content is mainly accounted for by a 2–3 times decrease in density.

As the density rises preceding the β_p-decline, the edge density gradients (and therefore pressure gradients) become very large ($dn_e/dr \sim 2\times10^{20}\mathrm{m}^{-4}$). The high–$n$ ballooning analysis given in Fig. 10 indicates that the pressure gradients close to the edge approach marginal stability, immediately preceding the ELM. The very outermost flux surfaces ($R \gtrsim 4.10$m) are however completely stable (ie. at the 'experimental' shear value there is no region of instability). It should be noted that there are significant experimental uncertainties in determining the edge pressure gradients. This ballooning analysis is based on the method of Greene and Chance [15] which allows the shear and pressure gradient to be varied at each flux surface. The marginal ballooning stability, shown in Fig. 10, is to be contrasted with normal H–mode operation in JET, where the edge pressure gradients are significantly below the ideal ballooning threshold [16]. It should be noted that the pressure gradients are also significantly below the ideal ballooning limit during the ELM's which occur shortly after the ICRF heating is applied. Thus it may be that the large ELM's immediately preceding β_p-declines (but not the earlier smaller ELM's) are triggered by an ideal ballooning instability. This conclusion is consistent with the reported marginal stability to ideal ballooning modes immediately preceding the giant (or type I) ELM's in DIII–D [17].

The multi-channel reflectometer [18] shows evidence for increased high frequency ($\sim$100kHz) density fluctuations near the plasma edge, as the time of the large ELM is approached. Figure 11 shows this result by comparing the power spectra at $n = 1.94\times10^{19}\mathrm{m}^{-3}$, for discharges where data is acquired during and 2.1 sec before the ELM. It can be seen that the high frequency activity increases significantly near the time of the ELM, perhaps indicating some high–n instability developing.

5 Summary and Discussion

High–β_p bootstrap current dominated plasmas have been produced in JET using ICRF heating. These results, which are the first to be corroborated by the polarimetry data, constitute the clearest

evidence to date for the existence of bootstrap current in JET.

In a typical high–β_p H-mode discharge, following the application of ICRF heating, ELM's initially occur. These ELM's cease after 1–2 seconds and a marked improvement in confinement occurs, which is manifested as a monotonic rise in plasma density. During this ELM–free phase the pressure rises up to $\beta_p \sim 2$ and the bootstrap fraction rises up to 70% ± 15% (for 1MA discharges). The ELM–free phase is terminated by a loss of H–mode and a rapid reduction in β_p, an event which is always initiated by a large ELM. There is a strong interaction with the ICRF antenna prior to this ELM, caused by the reduced plasma-antenna distance in H–mode and the poor match of the plasma boundary to antenna shape. Although the cause of the large ELM is not certain, there is evidence of increased high–n density fluctuations and an approach to the ideal ballooning stability boundary immediately preceding the ELM. In some discharges (notably those with $I_p = 1.5$MA) the cycle of β_p rising and loss of H-mode due to a large ELM may repeat itself several times.

It is interesting to contrast these results with those reported from JT–60 [4] where a comparable bootstrap fraction ($\sim$ 80%) occurs in NBI discharges. Superficially both JET and JT–60 show similar behaviour with comparable bootstrap fractions and the high–β_p phase being terminated by a rapid β_p–decline. However in JT–60 the NBI establishes a more peaked density profile and so the bootstrap current is relatively near to the magnetic axis. This causes the central–q to rapidly become non–monotonic and this in turn is thought to trigger an internal kink instability, leading to the β_p–decline. In contrast the β_p–decline in JET is caused by an edge instability and there is no apparent direct causal link with the bootstrap current. Thus the JET and JT60 results indicate a diverse range of behaviour which can occur in bootstrap dominated discharges and highlight the need for careful control of the density profile. Such a need for careful control of the density to establish stable bootstrap dominated reactors is central to the ARIES reactor designs [19].

Finally it is of interest to examine what the steady–state current density profiles in JET would have been if the β_p–decline had not occurred. At these temperatures steady–states under neo-classical resistive evolution are only achieved after a considerable time ($\sim$ 60s) and so the computationally efficient LARS 1-1/2D transport code [20] was used to compute these steady–states (though strictly, high values of β_p transgress the conventional tokamak ordering employed in the code). For these calculations the density profile was held fixed at that immediately preceding the β_p–decline and the code run to steady state. The resulting q–profile is shown in Fig. 12. It can be seen that for this case the central–q has risen through two, an event which would be expected to trigger internal MHD activity.

Acknowledgement

The Culham Laboratory authors were funded by the United Kingdom Department of Trade and Industry.

References

[1] R.J.Bickerton, J.W.Connor and J.B.Taylor, Nature (London), Phys Sci **229** (1971) 110.
[2] M.C.Zarnstorff, M.G.Bell, M.Bitter et al, Phys Rev Lett **60** (1988) 1306.
[3] C.D.Challis, J.G.Cordey, H.Hannen et al, Nucl Fusion **29** (1989) 563.
[4] S.Ishida, Y.Koide, T.Ozeki et al, Phys Rev Lett **68** (1992) 1531.

[5] J.S.Kim and J.M.Greene, Plasma Physics and Controlled Fusion **31** (1989) 1069.
[6] The JET team (presented by J.Jacquinot) Plasma Phys and Contr Fusion **33** (1991) 1657.
[7] M.F.F.Nave, D.J.Campbell et al, Nucl Fusion **31** (1991) 697.
[8] D.P.Schissel, J.C.DeBoo, K.H.Burrell et al, Nucl Fusion **31** (1991) 73.
[9] R.J.Goldston, D.C.McClune, H.H.Towner, S.L.Davis, R.J.Hawryluck and G.L.Schmidt, Jnrl Comp Phys **43** (1981) 61.
[10] D.P.O'Brien, L.L.Lao, E.R.Solano et al, Nucl Fusion **32** (1992) 1351.
[11] J.Blum, E.Lazzaro, J.O'Rourke, B.Keegan, and Y.Stephan, Nucl Fusion **30** (1990) 1475.
[12] S.P.Hirshman, Phys Fluids **21** (1978) 1295.
[13] L.A.Charlton, J.A.Holmes, V.E.Lynch, B.A.Carreras and T.C.Hender, Jrnl Comp Phys **86** (1982) 270.
[14] P.Smeulders, J.M.Adams, B.Balet et al, 17th European Conf on Plasma Phys and Contr Heating, **1** (1990) 323 (Publishers EPS Geneva).
[15] J.M.Greene and M.S.Chance, Nucl Fusion **21** (1981) 453.
[16] G.T.A.Huysmans, H.De.Blank, W.O.Kerner, J.P.Goedbloed and M.F.F.Nave, Proc of the Int Conf on Plasma Phys Innsbruck (1992), **1** (1992) 72 (Publishers EPS Geneva).
[17] P.Gohil, M.Ali-Mahdavi et al, Phys Rev Lett **61** (1988) 1603.
[18] R.Prentice, A.C.C.Sips, J.A.Fessey and A.E.Costley, 17th European Conf on Plasma Phys and Contr Heating, **4** (1990) 1503 (Publishers EPS Geneva).
[19] The ARIES Rector Study, University of California Los Angeles Report UCLA–PPG-1274 (1989).
[20] R.Fitzpatrick, C.G.Gimblett and R.J.Hastie, Plasma Phys and Contr Fusion, **34** (1992) 161.

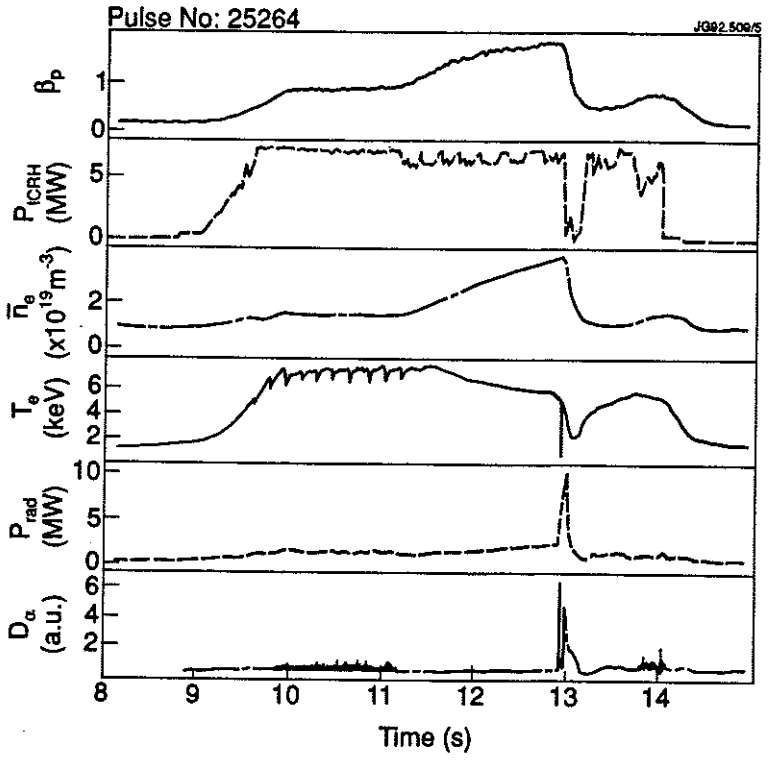

Fig. 1 Typical 1MA high-β_p discharge showing the evolution of the kinetic-β_p, coupled ICRF heating power (P_{ICRH}), line average electron density ($\bar{n}_e$), central electron temperature (T_e), radiated power (P_{rad}), and D_α-emission.

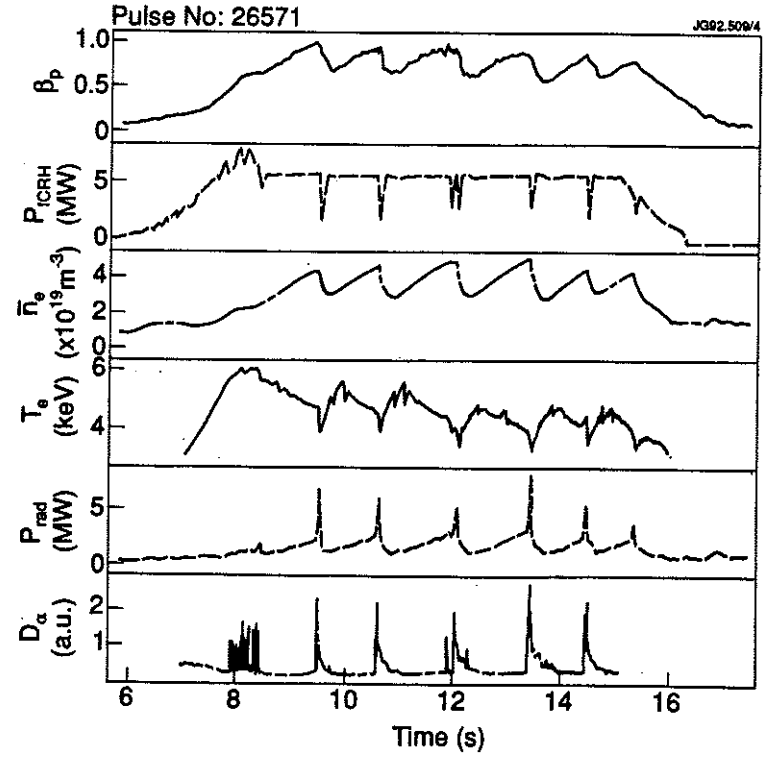

Fig. 2 As Fig. 1 but showing a 1.5MA discharge which exhibits a repeated cycle of β_p increasing and decreasing.

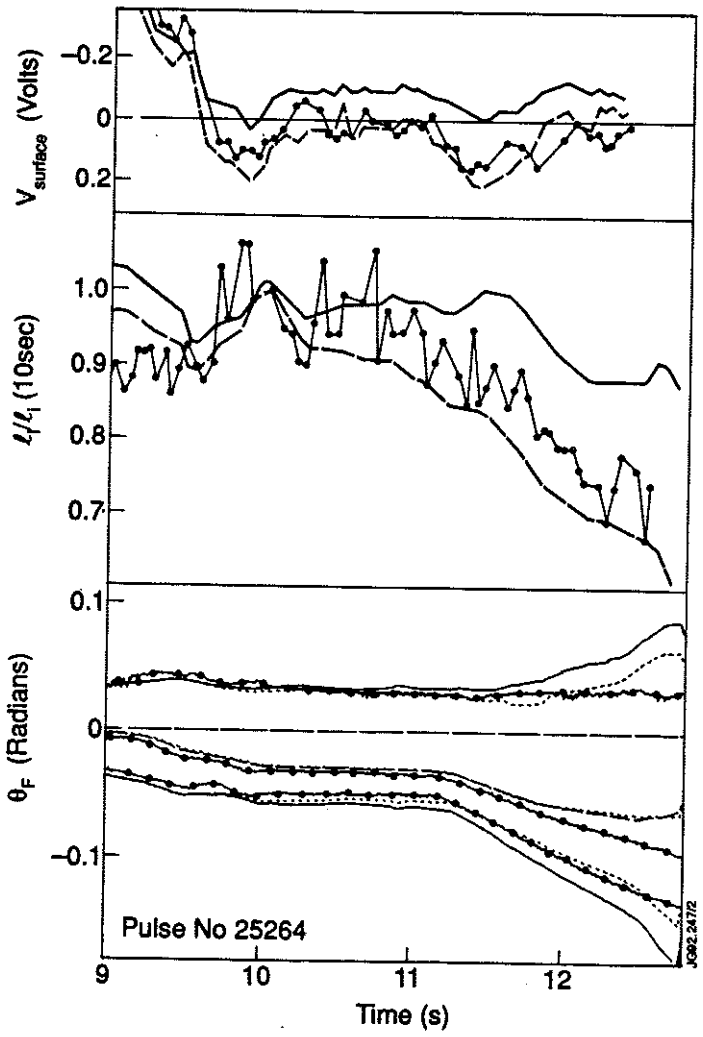

Fig. 3 Evolution of the loop voltage ($V_{surface}$), self inductance (l_i) and Faraday rotation angle (θ_F) for the discharge shown in Fig. 1. The three (θ_F) lines of sight from top to bottom are R =3.34, 3.02 and 2.9m respectively. Data (circles) and TRANSP calculations with (dashed lines) and without (solid lines) the bootstrap term included, are compared.

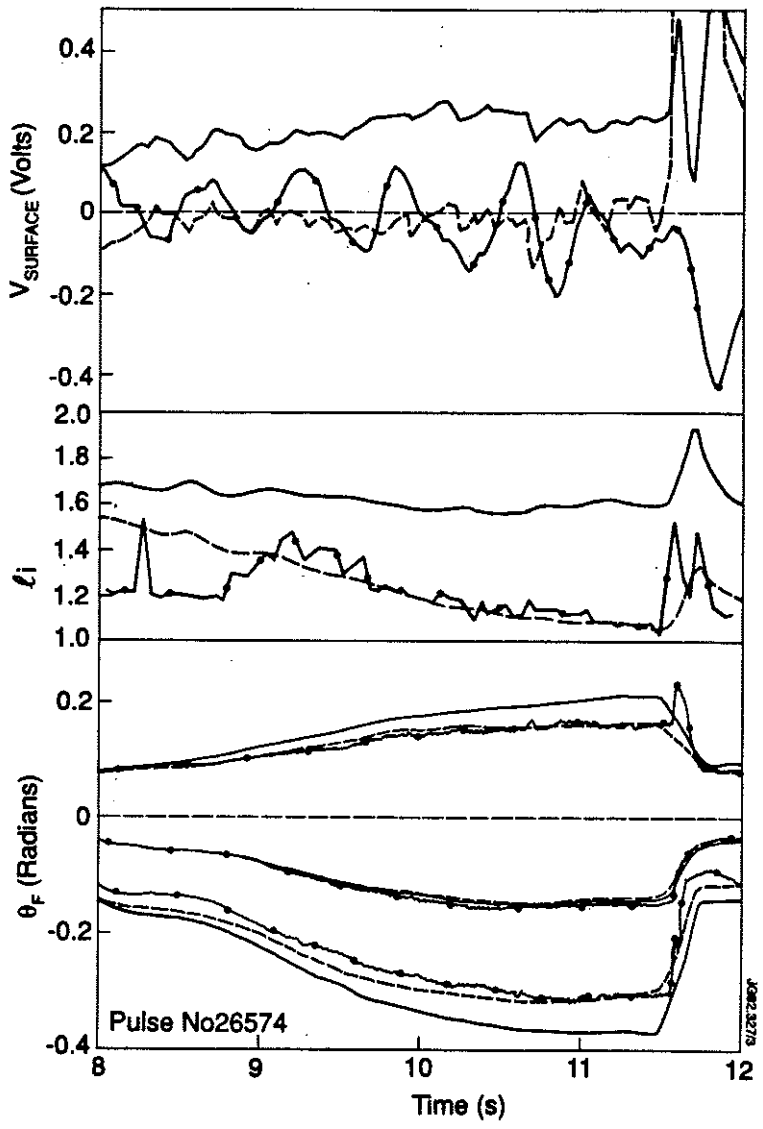

Fig. 4 As Fig. 3 but for a 1.5MA, 3.1T discharge.

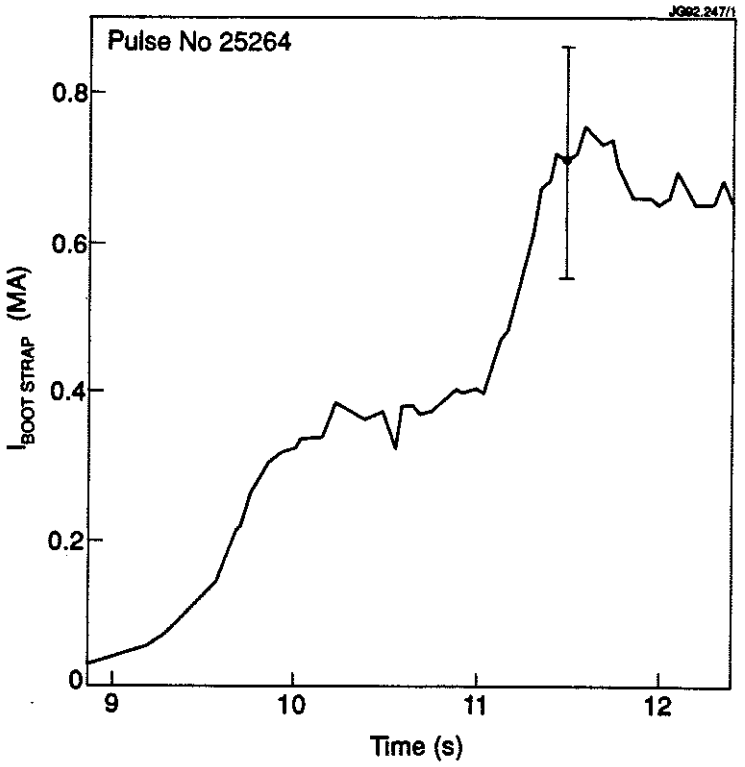

Fig. 5 Evolution of the bootstrap current calculated by TRANSP for the 1MA discharge of Figs. 1 and 3.

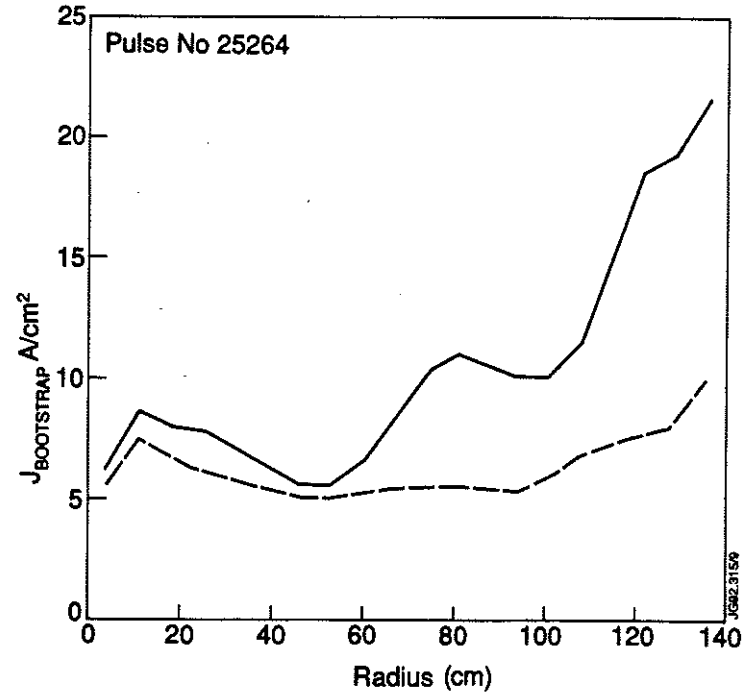

Fig. 6 Bootstrap current density profiles in the ELM (broken line, t =10.4s) and ELM-free phase (solid line, t =11.4s) calculated by TRANSP.

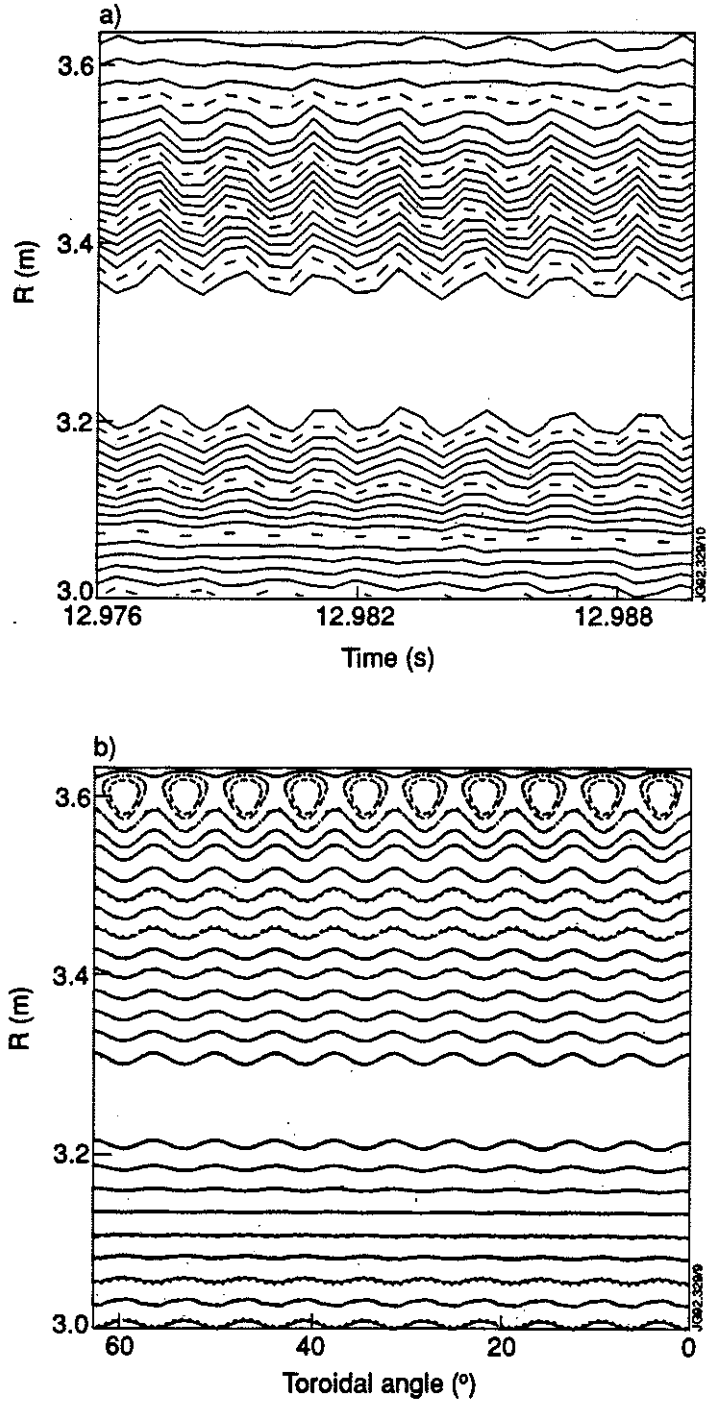

Fig. 7(a) ECE temperature contours in the horizontal mid-plane as a function of time (b) Theoretically computed flux surfaces in the horizontal mid-plane (distorted by $n = 1$ mode) as a function of toroidal angle. Both experiment (Fig. 7(a)) and theory (Fig. 7(b)) show phase inversions between $R = 3.0$ and 3.2m, no phase inversion across the magnetic axis ($R = 3.3m$) and a phase inversion between $R = 3.55$ and 3.65m.

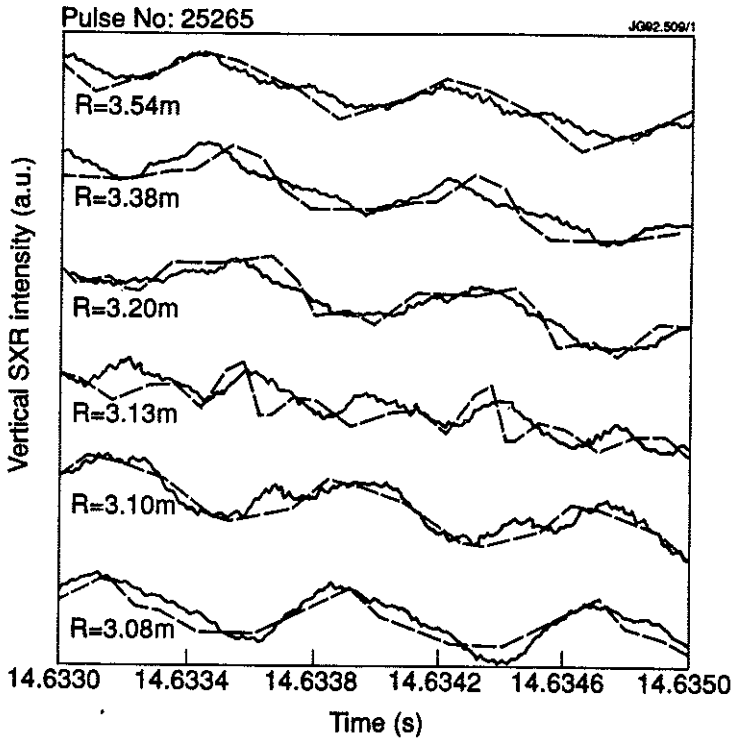

Fig. 8 Comparison between experimental (solid line) and theoretically reconstructed (broken line) central vertical SXR chords. The oscillations are due to the central $n = 1$ mode. An average downward drift has been added to the theoretical curves to facilitate comparison with experiment.

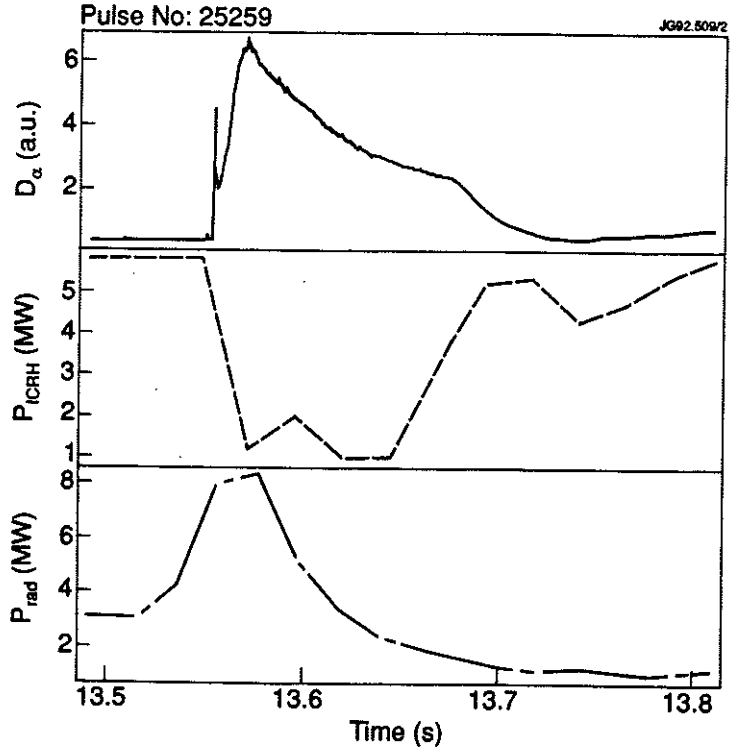

Fig. 9 $\dot{D}_\alpha$-emission, radiated power and coupled ICRH power for a 1MA discharge at the time of the β_p-decline.

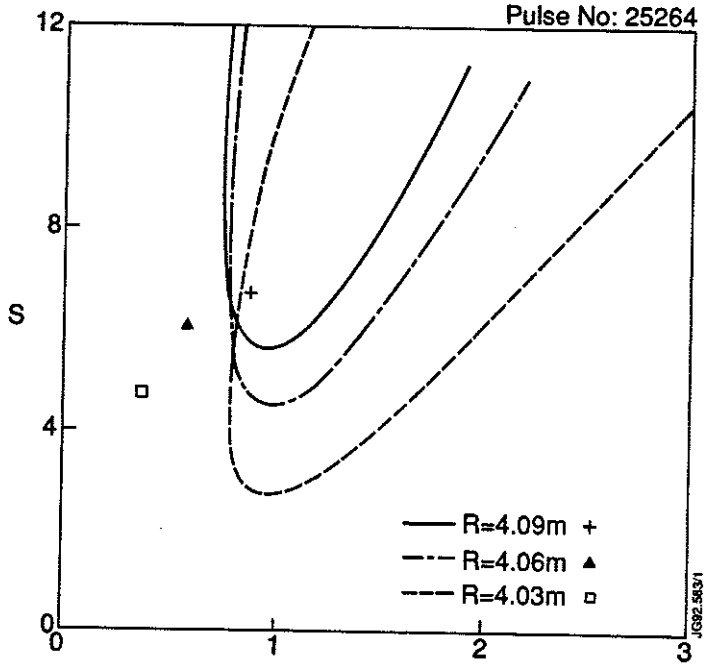

Fig. 10 Marginal stability boundaries in the $S[= r/q(dq/dR)]$ and $\alpha[= -(2\mu_0 r^2/RB_\theta^2)(dP/dR)]$ plane at three major radii; all quantities are evaluated at outboard midplane. The unstable region is in the upper right region enclosed by the stability boundaries. The symbols are experimental values just before β_p decline.

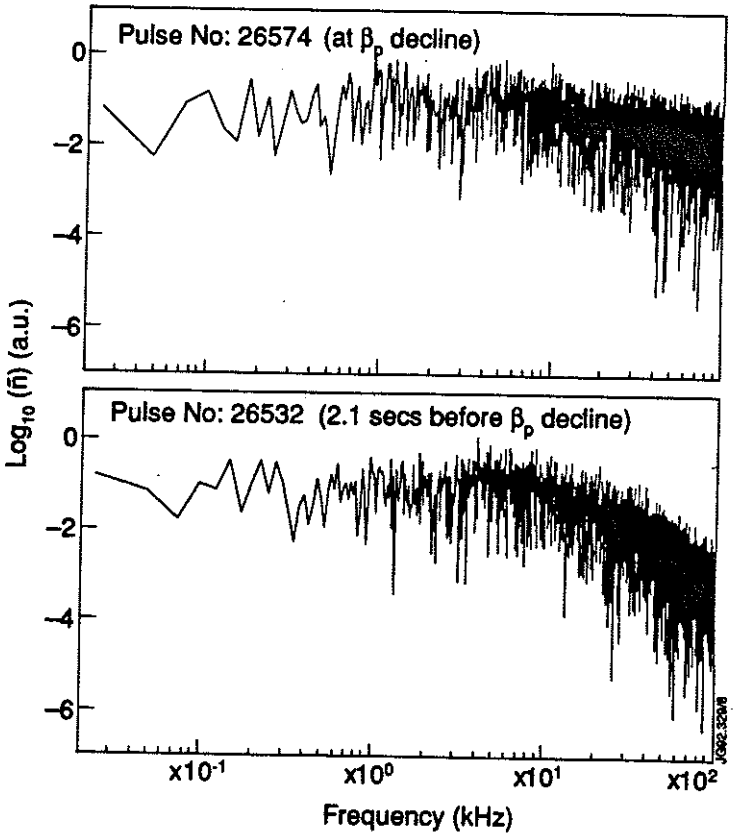

Fig. 11 Power spectra of density fluctuations for $n = 1.94 \times 10^{19} m^{-3}$. For shot 26574 data encompasses a β_p decline and for shot 26532 it is 2.1s before the decline.

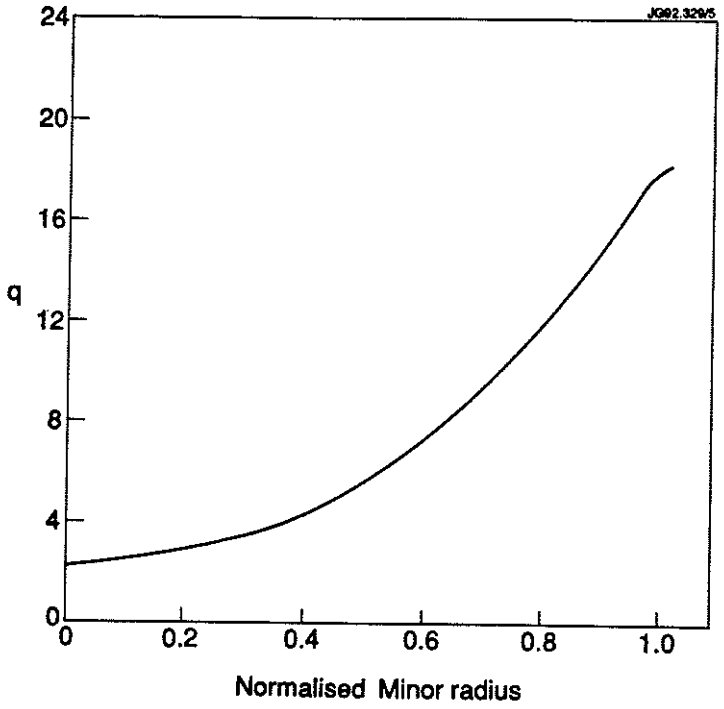

Fig. 12 Steady-state q-profile which would be obtained for the 1MA discharge of Figs. 1, 3 and 5 with density profile frozen at that immediately preceding the β_p-decline.

Appendix I

THE JET TEAM

JET Joint Undertaking, Abingdon, Oxon, OX14 3EA, U.K.

J.M. Adams[1], B. Alper, H. Altmann, A. Andersen[14], P. Andrew, S.Ali-Arshad, W. Bailey, B. Balet, P. Barabaschi, Y. Baranov, P. Barker, R. Barnsley[2], M. Baronian, D.V. Bartlett, A.C. Bell, G. Benali, P. Bertoldi, E. Bertolini, V. Bhatnagar, A.J. Bickley, D. Bond, T. Bonicelli, S.J. Booth, G. Bosia, M. Botman, D. Boucher, P. Boucquey, M. Brandon, P. Breger, H. Brelen, W.J. Brewerton, H. Brinkschulte, T. Brown, M. Brusati, T. Budd, M. Bures, P. Burton, T. Businaro, P. Butcher, H. Buttgereit, C. Caldwell-Nichols, D.J. Campbell, D. Campling, P. Card, G. Celentano, C.D. Challis, A.V.Chankin[23], A. Cherubini, D. Chiron, J. Christiansen, P. Chuilon, R. Claesen, S. Clement, E. Clipsham, J.P. Coad, I.H. Coffey[24], A. Colton, M. Comiskey[4], S. Conroy, M. Cooke, S. Cooper, J.G. Cordey, W. Core, G. Corrigan, S. Corti, A.E. Costley, G. Cottrell, M. Cox[7], P. Crawley, O. Da Costa, N. Davies, S.J. Davies[7], H. de Blank, H. de Esch, L. de Kock, E. Deksnis, N. Deliyanakus, G.B. Denne-Hinnov, G. Deschamps, W.J. Dickson[19], K.J. Dietz, A. Dines, S.L. Dmitrenko, M. Dmitrieva[25], J. Dobbing, N. Dolgetta, S.E. Dorling, P.G. Doyle, D.F. Düchs, H. Duquenoy, A. Edwards, J. Ehrenberg, A. Ekedahl, T. Elevant[11], S.K. Erents[7], L.G. Eriksson, H. Fajemirokun[12], H. Falter, J. Freiling[15], C. Froger, P. Froissard, K. Fullard, M. Gadeberg, A. Galetsas, L. Galbiati, D. Gambier, M. Garribba, P. Gaze, R. Giannella, A. Gibson, R.D. Gill, A. Girard, A. Gondhalekar, D. Goodall[7], C. Gormezano, N.A. Gottardi, C. Gowers, B.J. Green, R. Haange, A. Haigh, C.J. Hancock, P.J. Harbour, N.C. Hawkes[7], N.P. Hawkes[1], P. Haynes[7], J.L. Hemmerich, T. Hender[7], J. Hoekzema, L. Horton, J. How, P.J. Howarth[5], M. Huart, T.P. Hughes[4], M. Huguet, F. Hurd, K. Ida[18], B. Ingram, M. Irving, J. Jacquinot, H. Jaeckel, J.F. Jaeger, G. Janeschitz, Z. Jankowicz[22], O.N. Jarvis, F. Jensen, E.M. Jones, L.P.D.F. Jones, T.T.C. Jones, J-F. Junger, F. Junique, A. Kaye, B.E. Keen, M. Keilhacker, W. Kerner, N.J. Kidd, R. Konig, A. Konstantellos, P. Kupschus, R. Lässer, J.R. Last, B. Laundy, L. Lauro-Taroni, K. Lawson[7], M. Lennholm, J.Lingertat[13], R.N. Litunovski, A. Loarte, R. Lobel, P. Lomas, M. Loughlin, C. Lowry, A.C. Maas[15], B. Macklin, C.F. Maggi[16], G. Magyar, V. Marchese, F. Marcus, J. Mart, D. Martin, E. Martin, R. Martin-Solis[8], P. Massmann, G. Matthews, H. McBryan, G. McCracken[7], P. Meriguet, P. Miele, S.F. Mills, P. Millward, E. Minardi[16], R. Mohanti[17], P.L. Mondino, A. Montvai[3], P. Morgan, H. Morsi, G. Murphy, F. Nave[27], S. Neudatchin[23], G. Newbert, M. Newman, P. Nielsen, P. Noll, W. Obert, D. O'Brien, J. O'Rourke, R. Ostrom, M. Ottaviani, S. Papastergiou, D. Pasini, B. Patel, A. Peacock, N. Peacock[7], R.J.M. Pearce, D. Pearson[12], J.F. Peng[26], R. Pepe de Silva, G. Perinic, C. Perry, M.A. Pick, J. Plancoulaine, J-P. Poffé, R. Pohlchen, F. Porcelli, L. Porte[19], R. Prentice, S. Puppin, S. Putvinskii[23], G. Radford[9], T. Raimondi, M.C. Ramos de Andrade, M. Rapisarda[29], P-H. Rebut, R. Reichle, S. Richards, E. Righi, F. Rimini, A. Rolfe, R.T. Ross, L. Rossi, R. Russ, H.C. Sack, G. Sadler, G. Saibene, J.L. Salanave, G. Sanazzaro, A. Santagiustina, R. Sartori, C. Sborchia, P. Schild, M. Schmid, G. Schmidt[6], H. Schroepf, B. Schunke, S.M. Scott, A. Sibley, R. Simonini, A.C.C. Sips, P. Smeulders, R. Smith, M. Stamp, P. Stangeby[20], D.F. Start, C.A. Steed, D. Stork, P.E. Stott, P. Stubberfield, D. Summers, H. Summers[19], L. Svensson, J.A. Tagle[21], A. Tanga, A. Taroni, C. Terella, A. Tesini, P.R. Thomas, E. Thompson, K. Thomsen, P. Trevalion, B. Tubbing, F. Tibone, H. van der Beken, G. Vlases, M. von Hellermann, T. Wade, C. Walker, D. Ward, M.L. Watkins, M.J. Watson, S. Weber[10], J. Wesson, T.J. Wijnands, J. Wilks, D. Wilson, T. Winkel, R. Wolf, D. Wong, C. Woodward, M. Wykes, I.D. Young, L. Zannelli, A. Zolfaghari[28], G. Zullo, W. Zwingmann.

PERMANENT ADDRESSES

1. UKAEA, Harwell, Didcot, Oxon, UK.
2. University of Leicester, Leicester, UK.
3. Central Research Institute for Physics, Budapest, Hungary.
4. University of Essex, Colchester, UK.
5. University of Birmingham, Birmingham, UK.
6. Princeton Plasma Physics Laboratory, New Jersey, USA.
7. UKAEA Culham Laboratory, Abingdon, Oxon, UK.
8. Universidad Complutense de Madrid, Spain.
9. Institute of Mathematics, University of Oxford, UK.
10. Freien Universität, Berlin, F.R.G.
11. Royal Institute of Technology, Stockholm, Sweden.
12. Imperial College, University of London, UK.
13. Max Planck Institut für Plasmaphysik, Garching, FRG.
14. Risø National Laboratory, Denmark.
15. FOM Instituut voor Plasmafysica, Nieuwegein, The Netherlands.
16. Dipartimento di Fisica, University of Milan, Milano, Italy.
17. North Carolina State University, Raleigh, NC, USA
18. National Institute for Fusion Science, Nagoya, Japan.
19. University of Strathclyde, 107 Rottenrow, Glasgow, UK.
20. Institute for Aerospace Studies, University of Toronto, Ontario, Canada.
21. CIEMAT, Madrid, Spain.
22. Institute for Nuclear Studies, Otwock-Swierk, Poland.
23. Kurchatov Institute of Atomic Energy, Moscow, USSR
24. Queens University, Belfast, UK.
25. Keldysh Institute of Applied Mathematics, Moscow, USSR.
26. Institute of Plasma Physics, Academica Sinica, Hefei, P. R. China.
27. LNETI, Savacem, Portugal.
28. Plasma Fusion Center, M.I.T., Boston, USA.
29. ENEA, Frascati, Italy.

At 1st July, 1992